ACTUATORS

Semiseparated biphasic bicontinuous dielectric elastomer for high-performance artificial muscle

Xiaotian Shi[1,2]†, Jiang Zou[1,2]†, Peinan Yan[1,2], Rongtai Wan[3], Baoyang Lu[3]*, Guoying Gu[1,2]*, Xiangyang Zhu[1,2]*

Electrically driven dielectric elastomer artificial muscles represent a transformative advancement in the field of soft robotics. However, their output performance has encountered a bottleneck owing to the insufficient electromechanical sensitivity of dielectric elastomers. We present a hetero-cross-linking–induced phase separation strategy to design semiseparated biphasic bicontinuous dielectric elastomers with a high electromechanical sensitivity of 360 per megapascal. Our strategy harnesses varying silicone elastomer cross-linking mechanisms to form an interconnected dielectric phase within a soft mechanical phase in the resultant elastomers. These elastomer-based artificial muscles simultaneously exhibit high energy density and power density, as well as ultralong life span under low-driving fields. Applications involve a robotic arm with large stroke and untethered soft crawling robots with multimodal locomotion, showcasing their versatility.

Design of muscle-like soft actuators capable of converting electrical energy to mechanical energy is a challenge in the field of soft robotics (*1*–*5*), haptics (*6*–*8*), and prosthetics (*9*, *10*). Many types of deformable materials stimulated by electricity (*11*–*15*) have been developed with dielectric elastomers (e.g., acrylics and silicones). Sandwiched between two compliant electrodes under a specific voltage, a dielectric elastomer membrane is compressed in thickness and expanded in area (*16*) as a result of the electrostatic stress [known as Maxwell stress (*17*)]. Based on this working principle, the resultant membrane thickness deformation (z) under a specific electric field mainly relates to the relative dielectric constant (ε_r) and Young's modulus (Y) of the dielectric elastomer, i.e., $z \propto \varepsilon_r / Y$ (*18*).

It has been challenging to tailor the electromechanical sensitivity (termed as ε_r / Y) to improve the actuation performance of dielectric elastomers under lower electric fields. By increasing the relative dielectric constant ε_r, improvements have been achieved through filler composition (*19*), chemical modifications (*20*), and elastomeric network optimization (*21*). Although high performance has been reported, the electromechanical sensitivity is still generally within 110 MPa^{-1}. Another effective strategy to improve the electromechanical sensitivity is to reduce the Young's modulus Y. However, it remains challenging to achieve this, owing to the compromise in relative dielectric constant as well as other electromechanical parameters, such as breakdown electric field and life span (*22*).

Hetero-cross-linking–induced phase separation strategy

We present a hetero-cross-linking–induced phase separation strategy to design a semiseparated biphasic bicontinuous dielectric elastomer (SBE). Our strategy utilizes varying cross-linking mechanisms applied to two commercial silicone elastomers (i.e., Sylgard 170 and Elastosil P7676) to form an interconnected dielectric phase (D-Phase) within a very soft mechanical phase (M-Phase). The D-Phase of Sylgard 170 (with a high relative dielectric constant of ~3.9) is fabricated by high-density main-chain cross-linking of telechelic vinyl functionalized polydimethylsiloxane with a multihydrosilane (Si–H) functionalized cross-linker. At the same time, the M-Phase of Elastosil P7676 (with an ultralow Young's modulus of ~8 kPa) is achieved by low-density side-chain cross-linking of bottle-brush polydimethylsiloxane through hydrosilylation in the presence of a commercial platinum catalyst (figs. S1 to S5). The hetero-cross-linking mechanisms of both components lead to the creation of two distinct phases with blurred boundaries owing to the interpenetration of similar polydimethylsiloxane chains. This results in a semiseparated biphasic bicontinuous elastomer (Fig. 1A), which differs from the formation of the homogeneous dual-network elastomers (*23*, *24*).

We confirm the formation of the semiseparated bicontinuous phase structure through structural and morphological characterizations. X-ray computed tomography (XCT) enables the visualization of the heterogeneous biphasic bicontinuous topological structure through density difference between the D-Phase and M-Phase (Fig. 1B and fig. S6), which is different from homogeneous dual-network elastomers (no phase separation). Atomic force microscopy (AFM) phase imaging further verifies the formation of interconnected continuous biphasic network in micrometer scales compared with pure D-Phase and M-Phase (Fig. 1C and fig. S7). Moreover, AFM nanomechanical mapping reveals distinct Derjaguin–Muller–Toporov (DMT) modulus and phase angle between the D-Phase and M-Phase within our SBE (Fig. 1D). The phase structure (Fig. 1E) may also enhance other electromechanical properties. For example, the blurred phase boundaries can create ubiquitous dielectric barriers (*25*), thus improving the breakdown electric field.

We systematically investigated the mechanical and electrical properties of SBEs under varying feeding ratios and compared them with commonly utilized commercial silicone elastomers. Stress-strain testing, dynamic mechanical analysis, differential scanning calorimetry, and dielectric spectroscopy (Fig. 1, F and G, and figs. S8 to S10) indicate that SBE exhibits an intermediate Young's modulus, mechanical loss tangent, glass transition temperature (T_g), and dielectric constant between two components with pure D-Phase and M-Phase as control. Our SBE displays a reluctant increment in the Young's modulus, yet a rapid enhancement in dielectric constant with the increase of the content of the D-Phase. Typically, SBE with only 10% of the D-Phase (SBE-1) exhibits a Young's modulus (~10 kPa) that when compared with pure D-Phase (~1450 kPa) is slightly higher than pure M-Phase (~8 kPa) but substantially lower than that of other commonly used commercial materials (Fig. 1F and fig. S11). By contrast, as we can see from Fig. 1G and fig. S12, the relative dielectric constant of our SBE-1 is 3.6 (44% higher than the relative dielectric constant of pure M-Phase), resulting in an electromechanical sensitivity of 360 MPa^{-1} (see "Measurements" in supplementary materials, materials and methods). Furthermore, cyclic tensile tests show that our SBE exhibits almost negligible hysteresis across the small, intermediate, and large strains (30, 100, 150, and 200%), indicating that it has better elasticity and mechanical stability than those of the pure M-Phase and D-Phase (fig. S13). Therefore, our SBE shows the potential to overcome the viscoelasticity of acrylic-based dielectric elastomers (*9*, *26*), leading to an improved response speed.

To validate the general applicability and elucidate the underlying chemical mechanism of our hetero-cross-linking approach, we extended the material portfolio to a series of analogous silicone dielectric elastomer materials with hetero-cross-linking mechanisms. The materials examined include both commercially available systems (such as Ecoflex 0030 paired with Sylgard 184, and Silgel 612 paired with Sylgard 160) and customized vinyl-terminated/hydroxyl-terminated silicone elastomers. The chemical reactions and catalysts of our customized silicone elastomers are provided in fig. S14. All the resultant silicone elastomers exhibit a distinct semiseparated biphasic bicontinuous structure

[1]State Key Laboratory of Mechanical System and Vibration, School of Mechanical Engineering, Shanghai Jiao Tong University, Shanghai, China. [2]Shanghai Key Laboratory of Intelligent Robotics, Shanghai Jiao Tong University, Shanghai, China. [3]Jiangxi Provincial Key Laboratory of Flexible Electronics, Flexible Electronics Innovation Institute, Jiangxi Science and Technology Normal University, Nanchang, China. ***Corresponding author. Email: guguoying@sjtu.edu.cn (G.G.); luby@jxstnu.edu.cn (B.L.); mexyzhu@sjtu.edu.cn (X. Z.)**
†These authors contributed equally to this work.

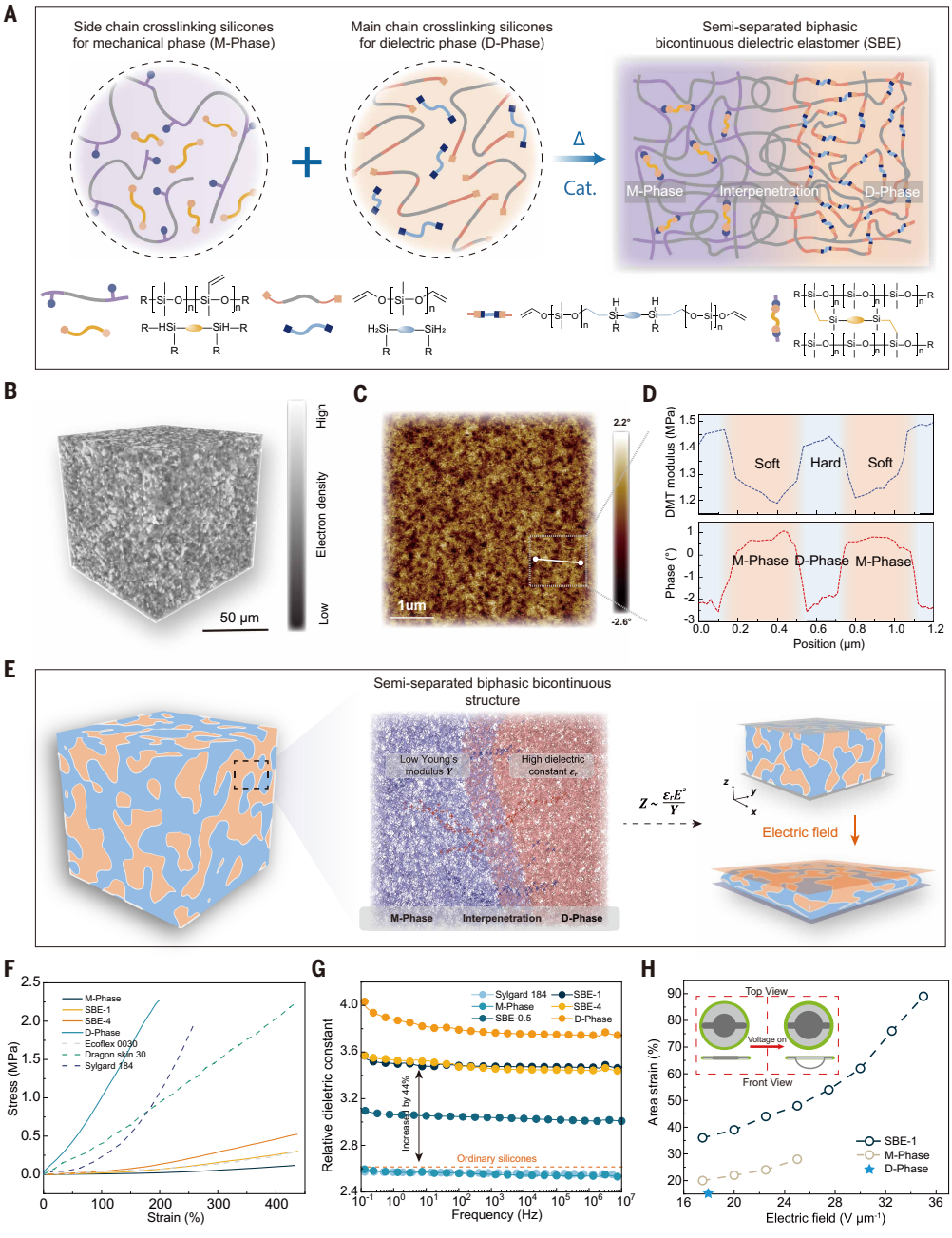

Fig. 1. Hetero-cross-linking–induced phase separation strategy and material properties. (**A**) The phase separation strategy of side-chain cross-linking type and main-chain cross-linking type. The side-chain cross-linking prepolymers undergo chemical cross-linking first under high temperatures and catalyst, precipitating an M-Phase in a topological mesh configuration. Concurrently, the unlinked main-chain cross-linking prepolymers migrate and aggregate, subsequently undergoing chemical cross-linking to precipitate a D-Phase, which fills the topology created by the elastic phase. (**B**) XCT and (**C**) AFM images demonstrate the biphasic bicontinuous structure of the SBE. (**D**) The phase angles and DMT modulus of the two phases show marked differences. (**E**) The SBE comprises M-Phase and D-Phase. The blurred phase boundaries (middle) create dielectric barriers leading to an enhanced breakdown electric field (right). (**F**) Stress-strain curves and (**G**) dielectric spectroscopy of SBEs and other commonly used silicone elastomers. (**H**) SBE-1 demonstrates superior electromechanical deformation performance, capable of achieving 90% area strain under 35 V μm^{-1} without prestretching, and displays enhanced electrical breakdown strength.

(fig. S15). Mechanical and dielectric testing reveals a considerable enhancement in electromechanical sensitivity, surpassing the performance of pure D-phase and M-phase elastomers (figs. S16 and S17). As a control, we investigated silicone elastomers with a homo-cross-linking mechanism. The resulting composite elastomers exhibited a uniform phase structure, and their electromechanical sensitivity represents a trade-off between the constituent materials (fig. S18). These findings highlight the material generality and versatility of our rational design strategy for high-performance dielectric elastomers.

We also characterized the electromechanical deformation ability of the SBE films with compliant electrodes. SBE-1 reaches a breakdown field strength of >35 V μm^{-1}, higher than that of both pure M-Phase at 25 V μm^{-1} and D-Phase at 18 V μm^{-1} (Fig. 1H). By integrating an ultralow Young's modulus and an enhanced dielectric constant and breakdown electric field, SBE-1 is capable of eliminating the electromechanical instability (fig. S19) and generating 90% area strain under a relatively lower electric field without prestretching (Fig. 1H, fig. S20, and movie S1), demonstrating exceptional electromechanical deformation capabilities (table S1).

High-performance SBE-based artificial muscles

To harness the properties of SBE, we first designed a kind of pure-shear SBE-based artificial muscle that consists of one single-layer SBE elastomer membrane coated on both sides with compliant electrodes (fig. S21). Under an excitation voltage, the pure-shear SBE-based artificial muscle elongates in the vertical direction, driving the load to produce a linear locomotion (Fig. 2A and movie S2). We characterized the linear strain and actuation stress of the pure-shear SBE-based artificial muscles with different feeding ratios. The results demonstrate that artificial muscles based on pure D-Phase or M-Phase struggle to generate effective electromechanical deformation and force because of their low electromechanical sensitivity and breakdown electric field (Fig. 2B and fig. S22). With our hetero-cross-linking–induced phase separation strategy, both the electromechanical sensitivity and breakdown electric field of our SBE are enhanced, enabling generation of >50% linear strain (SBE-1) with a strain rate of 400% s^{-1}. Additionally, Increasing the feed ratio reduces the electromechanical sensitivity of SBE, hindering its maximum linear strain.

We evaluated the energy density of our pure-shear SBE-based artificial muscles under different feeding ratios (Fig. 2C). The results show that under a low working frequency (<2 Hz), the maximum energy density of SBE-1, SBE-4, and SBE-6 reaches 209, 334, and 375 J kg^{-1}, respectively, which is generally higher than the energy density of pure M-Phase (85 J kg^{-1}) and D-Phase (23 J kg^{-1}) and the reported works

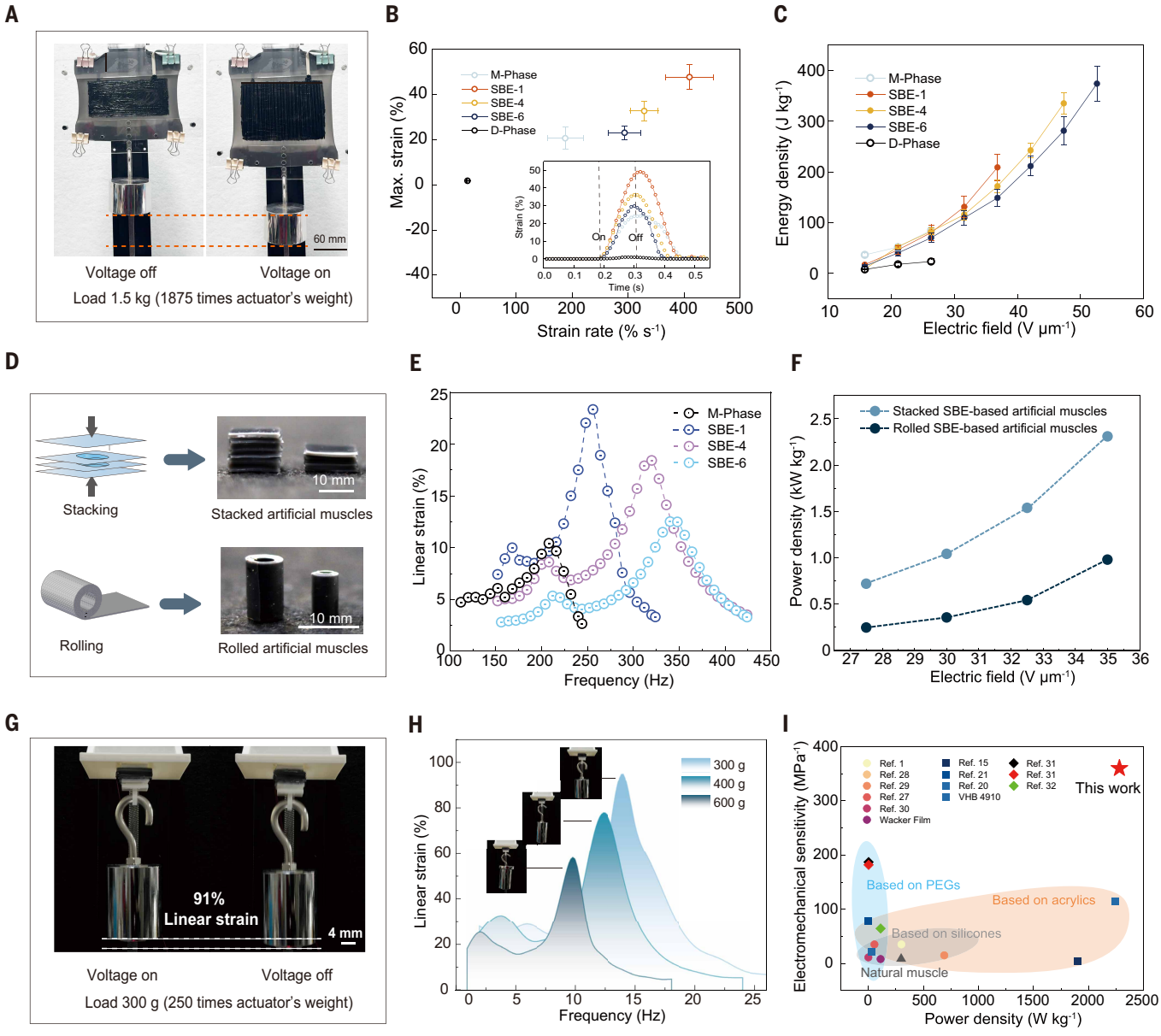

Fig. 2. Performances of SBE-based artificial muscles. (**A**) The pure-shear SBE-based artificial muscle exhibits a considerable linear strain under a 1.5-kg load. (**B**) The maximum strain and strain rate of the pure-shear SBE-based artificial muscle, with the inset illustrating the strain variation during a single actuation cycle. (**C**) Characterization of the energy density for the pure-shear SBE-based artificial muscle under different electric fields. (**D**) Schematic of the manufacturing process for artificial muscles. (**E**) Linear strain–frequency curves of SBE-based artificial muscles fabricated from SBEs with different feeding ratios. (**F**) Power density of stacked and rolled artificial muscles. Due to different driving directions, stacked artificial muscles demonstrate higher performance. (**G**) A stacked SBE-based artificial muscle with a height of 4.5 mm lifts a 300 g (250 times its weight) load by 4.1 mm (91% linear strain). (**H**) Linear strain–frequency curves of stacked SBE-based artificial muscles with suspended loads. (**I**) Comparison of electromechanical sensitivity and power density of SBE-based artificial muscles with other dielectric elastomer–based artificial muscles reported in the literature.

(table S2) (*9*, *13*, *15*, *20*). Under the same electric field, the energy density is negatively correlated to feeding ratios (Fig. 2C) because increasing feeding ratios leads to a decrease in electromechanical sensitivity. However, higher feeding ratios correspond to enhanced breakdown electric field, resulting in an increase in maximum energy density. By further analyzing their electromechanical efficiency, we found that the typical value is about 25%. The maximum electromechanical efficiency can exceed 60% by leveraging mechanical resonance (figs. S23 and S24).

We developed an efficient fabrication process to manufacture multilayered SBE-based artificial muscles (Fig. 2D), in which our SBE film is used as dielectric elastomer and single-wall carbon nanotube (SWCNT) thin film as the electrode (*27*). Typically, the SBE prepolymer solution is blade coated and cured to form a SBE film (~40 μm), covered with a thin SWCNT layer through a stamping transfer technique, and then coated with another SBE layer upon curing (figs. S25 and S26). Upon repeating such a procedure, we can achieve a multilayered sandwich structure of up to 15 layers. The multilayered sandwich structures are patterned into desired modules by laser cutting. Both negative and positive SWCNT electrodes are exposed and ready to connect with the power supply through conductive silicone electrodes. We further assemble such a structure into stacked or rolled SBE-based artificial muscles by dry stacking or simple rolling (figs. S27 and S28). Visualized by XCT imaging of their internal structures (fig. S29), both stacked and rolled SBE-based artificial muscles exhibit uniform thickness

and tight connections with an internal porosity <0.05%, confirming excellent structural integrity with negligible internal defects.

As-fabricated stacked artificial muscles can contract in thickness under an excitation voltage, whereas the rolled artificial muscles elongate along the axial direction. We further measured and compared the output performance of SBE-based artificial muscles with varying feeding ratios and geometric parameters (fig. S30). The actuation performance is fundamentally governed by the material's properties, as evidenced by the dependence of resonant frequency and strain amplitude on composition (Fig. 2E and fig. S31). Pure M-Phase–based artificial muscles demonstrate small linear strain (<10%) and low resonant frequency (200 Hz), primarily constrained by their low dielectric constant. Introducing a minor proportion of D-Phase (1:10, SBE-1) optimizes the electromechanical response by creating a semiseparated biphasic bicontinuous structure. This structure yields a superior combination of material properties (e.g., modulus and loss tangent) compared with pure-phase elastomers, which enhances the maximum linear strain to 25% (a 1.5-fold improvement) and increases the resonant frequency to 250 Hz. This enables actuators to not only resonate at higher frequencies but also to sustain large strain amplitudes under these conditions. By contrast, further increases in feeding ratios (e.g., SBE-3 and SBE-4) considerably elevate the Young's modulus without a commensurate increase in the dielectric constant (Fig. 1, F and G), leading to a marked deterioration in achievable linear strain. Among various feeding-ratio SBEs, the artificial muscle based on SBE-1 exhibits the best displacement output capability under high-frequency excitation and was thus used for subsequent tests of stacked and rolled artificial muscle (figs. S32 to S34). We found that by further analyzing the geometry effect through height optimization (in a range of 2 to 10 mm), the maximum response frequency can reach as high as 1500 Hz (figs. S35 and S36), which is superior to that reported in existing works (*1*, *15*, *20*). The blocked force density and power density results (Fig. 2F and figs. S37 to S39) show that stacked SBE–based artificial muscles (size of 8 mm by 8 mm by 3 mm, weight of 0.35 g) exhibit a maximum blocked force density of 21.76 kPa and a power density of 2250 W kg^{-1} at a high-frequency resonant state (>200 Hz) and an extremely low electric field of 35 V μm^{-1}, more than double that of rolled SBE-based artificial muscles (size of 80 mm by 5 mm by 240 μm before rolling; weight of 0.18 g).

Our SBE-based artificial muscles exhibit substantial load-driving capacity despite their ultralow Young's modulus (~10 kPa). Typically, the stacked SBE-based artificial muscles (height of 4.5 mm) are capable of repeatedly lifting a 300-g load (250 times their own weight) up to 4.1 mm (about 91% linear strain) with a maximum speed of 15 Hz (Fig. 2G and movie S3). If the load increases to 600 g (500 times their weight), the stroke of the stacked artificial muscles can still reach 2.7 mm (about 60% linear strain, Fig. 2H), demonstrating the powerful load-driving capacity of our artificial muscles (fig. S40). This performance exceeds natural muscles and reported dielectric elastomer–based artificial muscles (Fig. 2I and table S2) (*1*, *15*, *20*, *21*, *28*–*33*) and originates mainly from the improvement in electromechanical sensitivity.

Long-term stability and robustness

The inevitable performance degradation during long-term service is one of the major challenges for the application and commercialization of artificial muscles. Mechanical robustness, which is the output performance stability under mechanical deformation and high-number cyclic loading, is of particular concern for the life span of artificial muscles. We have conducted several fatigue tests with our SBEs and Pure M-Phase elastomers. The experimental results demonstrate that with the phase-separation microstructures (Fig. 3A), our SBE exhibits a fatigue threshold of 78 J m^{-2} (measured by the single-notch method). In comparison with pure M-Phase elastomer (21 J m^{-2}), the fatigue threshold is improved more than threefold (Fig. 3B). The underlying mechanism is likely due to the less-stretchable D-phase acting as a mechanical dissipater while the highly stretchable M-phase maintains the integrity and elasticity of the SBE (Fig. 3A), which is similar to previous results on tough double-network hydrogels (*34*, *35*). To further verify the mechanical robustness, we performed a 50,000-cycle validation test on a pinhole-cracked SBE at a constant strain of 50%, simulating the practical working conditions of SBE-based artificial muscles. Notably, SBE displays no obvious stress loss (<1%) after this test (Fig. 3C and fig. S41).

After being coated with carbon nanotube electrodes, our fabricated SBE-based artificial muscle exhibits a self-clearing capability (movie S4). This self-clearing process effectively reduces the structural defects

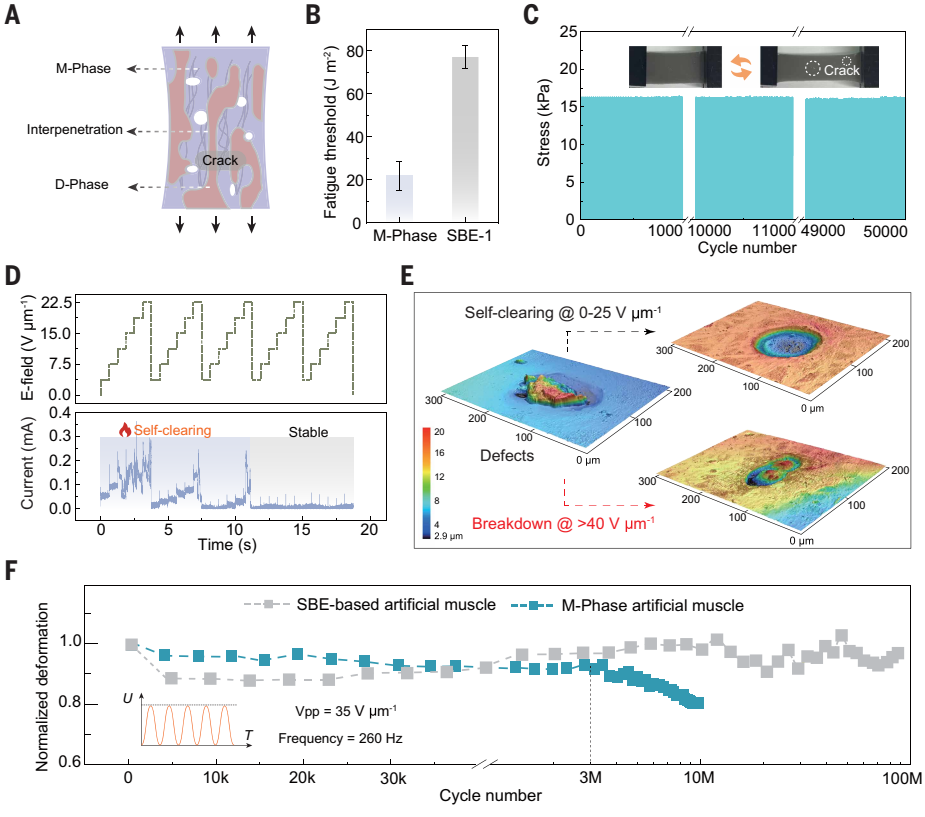

Fig. 3. Long-term stability and robustness of SBE-based artificial muscles. (**A**) Notches and pinholes are created on SBE to test its fatigue resistance and long-term stability. (**B**) Comparison of fatigue thresholds between M-Phase and SBE-1. The SBE-1 exhibits a threefold-higher fatigue threshold, attributed to the enhanced interfacial strength between the biphase. (**C**) Under conditions with notches and pinholes, SBE-1 shows no major stress loss after more than 50,000 stretching cycles. (**D**) Self-clearing is achieved with a stair voltage, with clearing completion indicated by zero current. (**E**) Confocal microscopy images of the SBE-based artificial muscle after self-clearing and destructive electrical breakdown, showing that self-clearing removes defects to form a well-defined pore, whereas excessive electric fields induce carbide accumulation leading to a short circuit. (**F**) Cyclic actuation testing of SBE-1 and M-Phase artificial muscle under an electric field of 35 V μm^{-1}. Vpp, peak-to-peak voltage; *U*, driving voltage; *T*, time.

and micropores within the artificial muscle by burning out low breakdown paths, thus facilitating the enhancement of output performance and long-term stability (*28*, *36*, *37*). During this process, a nonconductive region is formed, which isolates defects and allows the remaining functional areas to operate normally (fig. S42). By applying a cyclical stair voltage to perform this process and monitoring the current detection, we found that the actuation of our SBE-based artificial muscle causes transient erratic current during the first three cycles and then reaches a stabilized output performance as the current remains ~0 mA (Fig. 3D). We compared the surface morphology of SBE after self-clearing and destructive electric breakdown using confocal microscopy. The results reveal that the self-clearing process effectively remove defects within the SBE, forming a well-defined cavity. However, when the applied electric field is excessively high, considerable carbide accumulation occurs in the cavity, ultimately leading to a short circuit (Fig. 3E).

With its self-clearing capability and enhanced fatigue threshold, our SBE-based artificial muscle exhibits an enhanced output capacity and extended life span across both low and high working frequencies (such as more than 375,000 actuation cycles at 1 Hz and more than 100 million actuation cycles at 260 Hz under 35 V μm^{-1}) (Fig. 3F and figs. S43 to S46). By contrast, an artificial muscle fabricated with pure M-Phase suffers from performance attenuation upon only 3 million cycles (<80% after 10 million cycles; Fig. 3F). Moreover, the life span of other dielectric elastomer actuators based on commercial silicones is inferior to that of our SBE (table S3) (*15*, *20*, *28*, *38*–*40*).

Robotic arm with large stroke and high load capacity

We developed a robotic arm that consists of one rotational joint and four pure-shear SBE-based artificial muscles (Fig. 4A) (as detailed in "Fabrication" in supplementary materials, materials and methods). The pure-shear configuration is specifically selected for this bioinspired application because of its superior capability to generate large deformations coupled with high-force output under low-frequency operating conditions. These artificial muscles are divided into two antagonistic groups functioning as biceps and triceps, respectively.

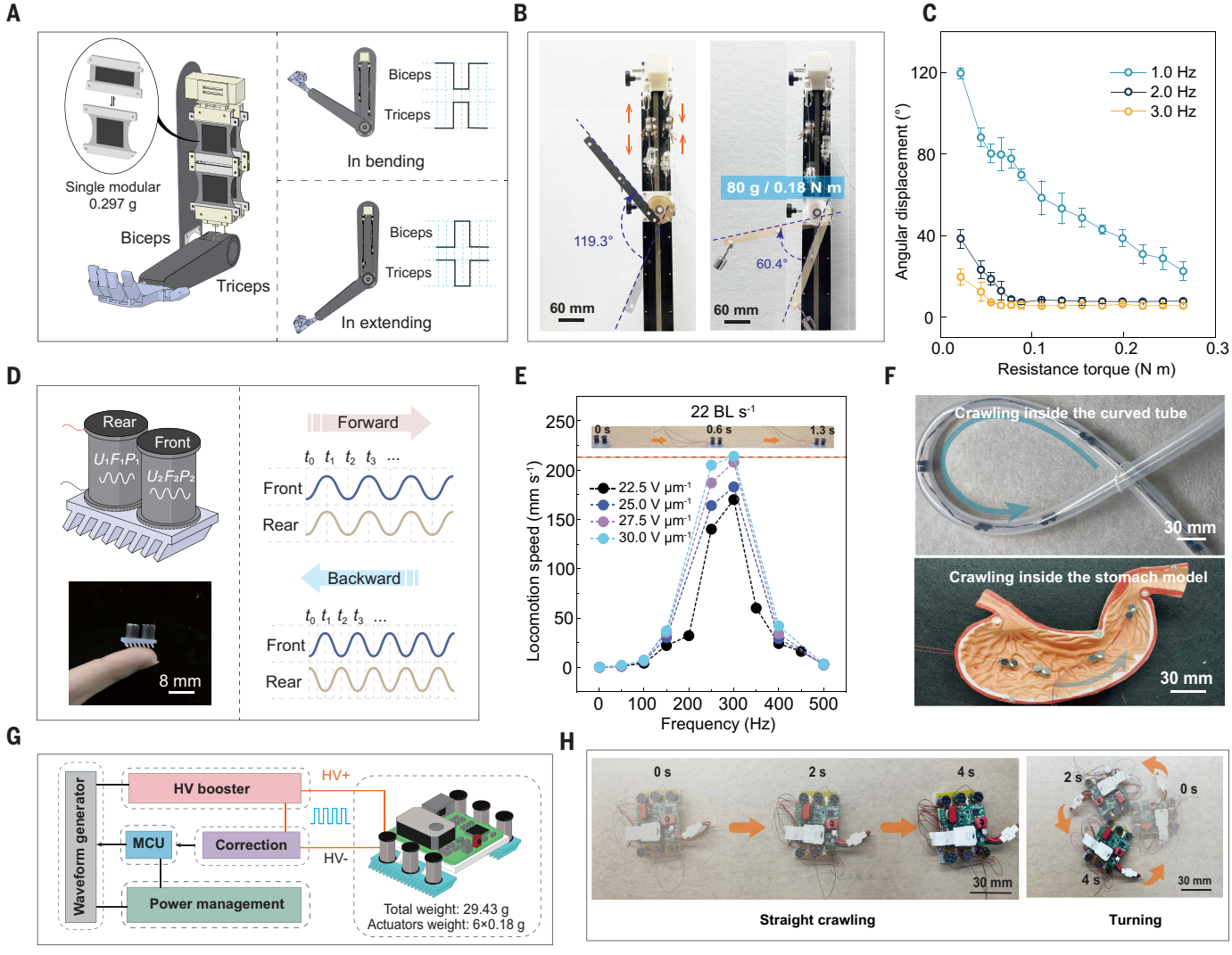

Fig. 4. Applications of SBE-based artificial muscles. (**A**) Design and working principle of a human-like robotic arm with four pure-shear SBE-based artificial muscles. (**B**) The robotic arm exhibits large stroke (119.3°) and high load capacity. (**C**) The angular displacement under different torque and frequency. (**D**) Design and gait implementation of an ultrafast soft crawling robot. Adjustments in movement direction and speed are achieved by modifying the driving frequency and phase differences between the front and rear artificial muscles. (**E**) The impact of electric field and driving frequency on the robot speed, with a maximum speed of up to 22 BL s^{-1}. (**F**) The robot crawling through curved tubes and a stomach model. (**G**) An infrared-controlled miniaturized high-frequency high-voltage drive circuit system and the design of an untethered robot. HV booster; high-voltage booster; MCU, microcontroller unit. (**H**) Demonstrations of crawling in a straight line and controlled turning.

When a high voltage is applied to the biceps, the robotic arm extends because the biceps elongate and the triceps contract. Conversely, the arm bends when the triceps are actuated. By alternately actuating biceps and triceps, we found that the angular displacement is proportional to the applied electric field (fig. S47) and that its maximum value can reach 119.3° (Fig. 4B and movie S5). We characterized the load capacity of the robotic arm by measuring the angular displacement under different resistance torques and actuation frequencies. The results demonstrate that although the effective weight of the four pure-shear SBE-based artificial muscles is <1.2 g, they can output a maximum torque of 0.24 N m, enabling the robotic arm to lift an 80-g load by 60.4° (Fig. 4C and movie S5) and chop through various obstacles (fig. S48 and movie S6). Lastly, we subjected the entire robotic arm system to more than 40,000 cycles of testing, during which it consistently remained stable and showed no performance degradation (fig. S49).

Multimodal and ultrafast robots with untethered capability

We designed and fabricated a soft crawling robot capable of multimodal locomotion (Fig. 4D and movie S7). The design comprises two SBE-based artificial muscles affixed to a flexible substrate with directional rectangular feet array (fig. S50). Under the same excitation voltage, SBE-based artificial muscles concurrently generate potent vibration that is converted into fast crawling via the anisotropic feet. The robot can execute hundreds of forward jumps within 1 s. The maximum crawling speed reaches 22 body lengths per second (BL s^{-1}) at a frequency of 300 Hz and a field strength of 30 V μm^{-1} (Fig. 4E, fig. S51 and movie S8). Upon implementing a phase delay in the rear artificial muscles under high frequency, we observed that the resulting asynchronous vibration facilitates a backward crawling gait (fig. S52 and movie S7), reaching a maximum speed of 40 mm s^{-1} with a phase difference of $T/2$ (T represents period of the excitation voltage) and a frequency of 450 Hz (movie S8). Leveraging its inherent softness and superior performance, the soft crawling robot can maneuver through curved tubes and navigate within a rugged stomach model (Fig. 4F and movies S9 and S10), showcasing its bioinspired adaptability to complex terrains and environments.

The low-driving electric field required for SBE-based artificial muscles paves the way for untethered applications. We developed an untethered soft crawling robot (Fig. 4G and figs. S53 and S54) integrating with a boost module, a microcontroller unit, an infrared wireless receiver, a calibration unit, and a battery. Although the total weight of the untethered robot reaches 29.43 g, it is powered by only six artificial muscles (weight of 6 × 0.18 g). This design enables both crawling and turning (Fig. 4H and movie S11). The design and integration of an untethered robotic system, traditionally a challenge in the deployment of dielectric elastomer actuators (*41*), are addressed by utilizing our SBE-based artificial muscles, which show superior output performance under a low-driving electric field.

Conclusions

This work presents a class of SBE with high electromechanical sensitivity through the hetero-cross-linking–induced phase separation strategy. After characterizing the mechanical and electrical properties of SBE under varying feeding ratios with commercially available silicone elastomers, we developed an efficient fabrication process to fabricate SBE-based artificial muscles that can synchronously exhibit high actuation performance in energy density, power density, response speed, electromechanical efficiency, and life span. We demonstrate a robotic arm and multimodal soft crawling robots that show high energy density and untethered capability. These advancements hold promise for the next generation of electrically driven soft robots that require enhanced output performance, ultralong life span, and excellent integrity.

REFERENCES AND NOTES

1. Y. Chen *et al.*, *Nature* **575**, 324–329 (2019).
2. G. Li *et al.*, *Nature* **591**, 66–71 (2021).
3. C. Tang *et al.*, *Sci. Robot.* **7**, eabm8597 (2022).
4. X. Ji *et al.*, *Sci. Robot.* **4**, eaaz6451 (2019).
5. G. Gu, J. Zou, R. Zhao, X. Zhao, X. Zhu, *Sci. Robot.* **3**, eaat2874 (2018).
6. G. Grasso, S. Rosset, H. Shea, *Adv. Funct. Mater.* **33**, 2213821 (2023).
7. E. Leroy, R. Hinchet, H. Shea, *Adv. Mater.* **32**, e2002564 (2020).
8. X. Ji *et al.*, *Adv. Funct. Mater.* **31**, 2006639 (2021).
9. M. Duduta, E. Hajiesmaili, H. Zhao, R. J. Wood, D. R. Clarke, *Proc. Natl. Acad. Sci. U.S.A.* **116**, 2476–2481 (2019).
10. J. Ham *et al.*, *Adv. Mater. Technol.* **8**, 2200903 (2023).
11. R. Pelrine, R. Kornbluh, Q. Pei, J. Joseph, *Science* **287**, 836–839 (2000).
12. C. Keplinger *et al.*, *Science* **341**, 984–987 (2013).
13. E. Acome *et al.*, *Science* **359**, 61–65 (2018).
14. X. Dong *et al.*, *Sci. Robot.* **6**, eabe3950 (2021).
15. Y. Shi *et al.*, *Science* **377**, 228–232 (2022).
16. L. An, F. Wang, S. Cheng, T. Lu, T. J. Wang, *Smart Mater. Struct.* **24**, 035006 (2015).
17. T. Lu, C. Ma, T. Wang, *Extreme Mech. Lett.* **38**, 100752 (2020).
18. Z. Suo, *Acta Mech. Solida Sin.* **23**, 549–578 (2010).
19. Y. Jiang *et al.*, *Adv. Mater.* **35**, e2300246 (2023).
20. W. Feng *et al.*, *Nat. Commun.* **15**, 4222 (2024).
21. L. J. Yin *et al.*, *Nat. Commun.* **12**, 4517 (2021).
22. L. J. Romasanta, M. A. Lopez-Manchado, R. Verdejo, *Prog. Polym. Sci.* **51**, 188–211 (2015).
23. J. Y. Sun *et al.*, *Nature* **489**, 133–136 (2012).
24. J. P. Gong, Y. Katsuyama, T. Kurokawa, Y. Osada, *Adv. Mater.* **15**, 1155–1158 (2003).
25. M. Yang *et al.*, *Nat. Nanotechnol.* **19**, 588–603 (2024).
26. G. Gu, U. Gupta, J. Zhu, L. Zhu, X. Zhu, *IEEE Trans. Robot.* **33**, 1263–1271 (2017).
27. W. Yuan *et al.*, *Adv. Mater.* **20**, 621–625 (2008).
28. H. Zhao *et al.*, *Adv. Funct. Mater.* **28**, 1804328 (2018).
29. S. Kim *et al.*, *Sci. Robot.* **8**, eadf4278 (2023).
30. S. Xu, Y. Chen, N. P. Hyun, K. P. Becker, R. J. Wood, *Proc. Natl. Acad. Sci. U.S.A.* **118**, e2103198118 (2021).
31. P. Huang, H. Fu, M. W. M. Tan, Y. Jiang, P. S. Lee, *Adv. Mater. Technol.* **9**, 2301642 (2023).
32. D. Yang *et al.*, *J. Mater. Chem. A Mater. Energy Sustain.* **3**, 9468–9479 (2015).
33. D. Yang *et al.*, *Compos. Sci. Technol.* **155**, 160–168 (2018).
34. X. Zhao, *Soft Matter* **10**, 672–687 (2014).
35. Y. Zhou *et al.*, *J. Mech. Phys. Solids* **153**, 104483 (2021).
36. Z. Peng, Y. Shi, N. Chen, Y. Li, Q. Pei, *Adv. Funct. Mater.* **31**, 2008321 (2021).
37. S. Jiang, C. Tang, X. J. Liu, H. Zhao, *Adv. Eng. Mater.* **24**, 2101017 (2022).
38. F. B. Albuquerque, H. Shea, *Smart Mater. Struct.* **30**, 125022 (2021).
39. P. Caspari, S. J. Dünki, F. A. Nüesch, D. M. Opris, *J. Mater. Chem. C Mater. Opt. Electron. Devices* **6**, 2043–2053 (2018).
40. Z. Ren *et al.*, *Adv. Mater.* **34**, e2106757 (2022).
41. S. I. Rich, R. J. Wood, C. Majidi, *Nat. Electron.* **1**, 102–112 (2018).

ACKNOWLEDGMENTS

We thank the following individuals for their valuable contributions and assistance throughout this research: W. Wang and J. Cao for chemical analysis; L. Wang for fatigue tests and analysis; L. Zhang for XCT imaging; Z. Qin and J. Feng for the assistance in thin film preparation; and X. Chen for the discussion of the dynamic model. We also thank the support of the Xplorer Prize. **Funding:** This work was supported by the National Key R&D Program of China (grant no. 2024YFB4707504); the National Natural Science Foundation of China (grant nos. 52025057, 91948302, and 52275024); and the State Key Laboratory of Mechanical System and Vibration (grant MSVZD202401). **Author contributions:** Conceptualization: X.S., J.Z., B.L., G.G., X.Z.; Funding acquisition: G.G., X.Z.; Investigation: X.S., P.Y., R.W.; Methodology: X.S., J.Z., B.L.; Project administration: J.Z., B.L., G.G., X.Z.; Supervision: G.G., X.Z.; Visualization: X.S.; Writing – original draft: X.S. Writing – review & editing: X.S., J.Z., B.L., G.G., X.Z. **Competing interests:** The authors declare that they have no competing interests. **Data and materials availability:** All data are available in the main text or the supplementary materials. Sources, synthesis and characterization of all materials are described in the methods section.

SUPPLEMENTARY MATERIALS

science.org/doi/10.1126/science.adr3521
Materials and Methods; Figs. S1 to S54; Tables S1 to S3; References (*42*–*45*); Movies S1 to S11

Submitted 27 June 2024; accepted 31 October 2025

10.1126/science.adr3521